Influence of Cell Geometry on Division-Plane Positioning

Nicolas Minc,[1,3,4,*] David Burgess,[2,3] and Fred Chang[1,3]
[1]Department of Microbiology and Immunology, Columbia University College of Physicians and Surgeons, 701 W168th Street, New York, NY 10032, USA
[2]Department of Biology, Boston College, 528 Higgins Hall, 140 Commonwealth Avenue, Chestnut Hill, MA 02167-3811, USA
[3]Marine Biological Laboratory, 7 MBL Street, Woods Hole, MA 02543, USA
[4]Present address: Institut Curie, UMR 144 CNRS/IC, 26 rue d'Ulm, 75248 Paris Cedex 05, France
*Correspondence: nicolas.minc@curie.fr
DOI 10.1016/j.cell.2011.01.016

SUMMARY

The spatial organization of cells depends on their ability to sense their own shape and size. Here, we investigate how cell shape affects the positioning of the nucleus, spindle and subsequent cell division plane. To manipulate geometrical parameters in a systematic manner, we place individual sea urchin eggs into microfabricated chambers of defined geometry (e.g., triangles, rectangles, and ellipses). In each shape, the nucleus is positioned at the center of mass and is stretched by microtubules along an axis maintained through mitosis and predictive of the future division plane. We develop a simple computational model that posits that microtubules sense cell geometry by probing cellular space and orient the nucleus by exerting pulling forces that scale to microtubule length. This model quantitatively predicts division-axis orientation probability for a wide variety of cell shapes, even in multicellular contexts, and estimates scaling exponents for length-dependent microtubule forces.

INTRODUCTION

The orientation of the division plane is a key element in the generation of a multicellular organism. During development, cells adopt a wide variety of geometrical configurations including spherical, ellipsoidal, and polyhedral shapes. Cell shape is thought to dictate the orientation of the division plane in many systems (Concha and Adams, 1998; Gray et al., 2004; O'Connell and Wang, 2000; Strauss et al., 2006; Thery and Bornens, 2006). This effect may guide the polarity of the initial cleavages in many developing embryos (Jenkinson, 1909). The correlation of the division plane with cell shape is described in Hertwig's empirical rule, also referred to as the "long axis rule" (Hertwig, 1884): "The two poles of the division figure come to lie in the direction of the greatest protoplasmic mass." The mechanism of nuclear and spindle positioning is now known to be a dynamic process that involves motor proteins, pulling and/or pushing forces from the microtubule (MT) and/or actin cytoskeletons (Grill and Hyman, 2005; Kunda and Baum, 2009; Reinsch and Gonczy, 1998; Wuhr et al., 2009). Depending on cell type, the division plane can be set by the orientation of the nucleus during interphase or early prophase or may be modified by rotation or movement of the spindle during anaphase. How these force-generating systems globally sense the shape and dimensions of the cell remains an outstanding question.

The single-cell sea urchin zygote is an attractive cell type for studying the effects of cell geometry. To date, many well-characterized systems for studying spindle positioning are in cells that exhibit asymmetric division, such as in *C. elegans* or *S. cerevisiae*, or in adherent mammalian cells. In these cell types, polarity cues or cell adhesion patterns appear to override geometric cues (Carminati and Stearns, 1997; Grill et al., 2001; Thery et al., 2005). In contrast, sea urchin zygotes are nonadherent, divide symmetrically, and appear to lack extrinsic polarity cues. These are spherical cells that have a highly reproducible cell size and cell-cycle timing. They have been used extensively in seminal studies in cytokinesis using physical manipulation approaches (Rappaport, 1996).

Here, we introduce the use of microfabricated wells to manipulate cell geometry parameters in a systematic and quantitative manner. By placing the sea urchin eggs into these chambers, we can mold them into highly reproducible series of cell shapes. In contrast to traditional physical manipulation methods on single cells, this approach allows for rapid acquisition of large datasets suitable for quantitative analysis. We find that the "long axis rule" does not apply for certain cell shapes. We develop a computational model that fully predicts the preferred division plane and the probability that this axis will be chosen for any given cell shape. This work demonstrates that cell shape sensing can be explained by a simple mechanism based upon microtubule length-dependent forces.

RESULTS

Manipulation of Cell Shape using Microfabricated Chambers

To control the geometry of sea urchin zygotes, we devised polydimethylsiloxane (PDMS) microfabricated chambers in which single eggs could be pushed into a variety of defined shapes

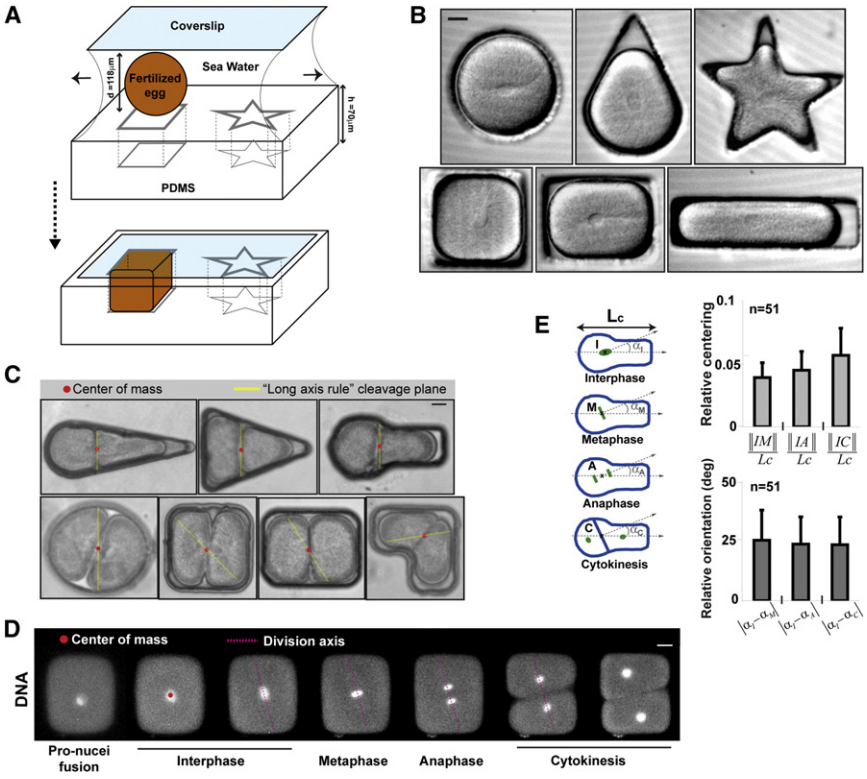

Figure 1. Controlling Cell Shape of Sea Urchin Embryos using Microfabricated Chambers

(A) Use of microfabricated PDMS wells for manipulating the shape of sea urchin embryos. Fertilized eggs are placed into wells of different shapes that are designed all to be the volume of an egg. The depth of the chambers (h) is smaller than the egg diameter (d) so that the egg is slightly flattened into its new geometry.

(B) Differential interference contrast (DIC) pictures of eggs in chambers adopting different geometries.

(C) Division-plane positioning in cells with different geometries. Cells of different shapes were introduced into wells and then assayed for division-plane positioning. The "long axis rule" predicts that cells will divide at the center of cell mass at an axis perpendicular to the long axis at this center. The cells in the top row follow this rule, but the cells in the bottom row do not.

(D) Time-lapse sequence of an embryo shaped in a rectangular chamber, from 15 min after fertilization to completion of cytokinesis. DNA was stained with Hoechst. Note the early centering of the zygote nucleus after pronuclei migration and fusion, and the elongation of the interphase nucleus along the future division axis.

(E) The orientation of the interphase nucleus predicts the future spindle axis and division plane in these cells. The relative centering and orientation at metaphase (M), anaphase (A), and cytokinesis (C) relative to interphase (I) are computed as indicated in the figure from time-lapse sequences. Error bars represent standard deviations.

Scale bars, 20 μm. See also Figure S1, Figure S2, and Movie S1.

(Minc et al., 2009b) (Figure 1A and Figure S1A available online). The total volume of each chamber was kept similar to the egg volume whereas the height was smaller than the egg diameter, so that the egg was slightly flattened into its new shape, allowing a bidimensional description of the process (see below). Cells were malleable and could form relatively sharp angles (down to 5–10 μm local radii of curvature), although further deformation was limited, probably because of cortical tension (Figure 1B). By removing sea water between the PDMS array and the top coverslip, we could cause the eggs to enter the chamber and change their shape in 1–5 min (Figure 2A). The embryos were surrounded by sea water and were not deprived of oxygen, as PDMS is gas permeable. In all shapes assessed, cells went on to divide within the chambers with normal timing for at least 24 hr (Figure S1B), indicating that their general physiology was not grossly perturbed.

Cell Shape Dictates Division-Plane Positioning during Interphase

We monitored the positioning and orientation of the division plane in many different shapes. In some shapes, cells divided in a plane at the cytoplasmic center perpendicular to the longest axis of the cell at this center. However, in other cases, we found exceptions to the long axis rule. Cells often divided at an angle different from that perpendicular to the cell's longest axis, for instance in an ellipse with a small aspect ratio in which the long axis was not well defined. The rule also did not apply well to shapes such as squares or rectangles. Rectangular cells usually did not divide along the long axis, which is the diagonal in this shape, but rather along the longest axis of symmetry (Figure 1C and Figure S1C).

To gain more insight into this process, we performed time-lapse imaging of embryos inside chambers going through the first cell cycle (from typically 20 min after fertilization to the end of cytokinesis). We imaged chromosomes stained with DNA dye Hoechst 33342 to track cell-cycle transitions and determine the positions and orientations of nuclei and mitotic spindles. Upon fertilization, the sperm nucleus, which brings the centrosomal material (Holy and Schatten, 1997), migrates toward the cytoplasmic center while pulling the female nuclei at the same time and is centered upon nuclear fusion (Hamaguchi and Hiramoto, 1986). We found that the zygote nucleus was centered within 5% of the cytoplasmic center of mass of the cell in all shapes assessed. In 92.5% of cases (n = 80), the interphase nucleus was clearly elongated along a stable and specific axis. After nuclear envelope breakdown, the mitotic spindle was aligned along this same axis throughout metaphase, anaphase, and telophase. The cleavage furrow then

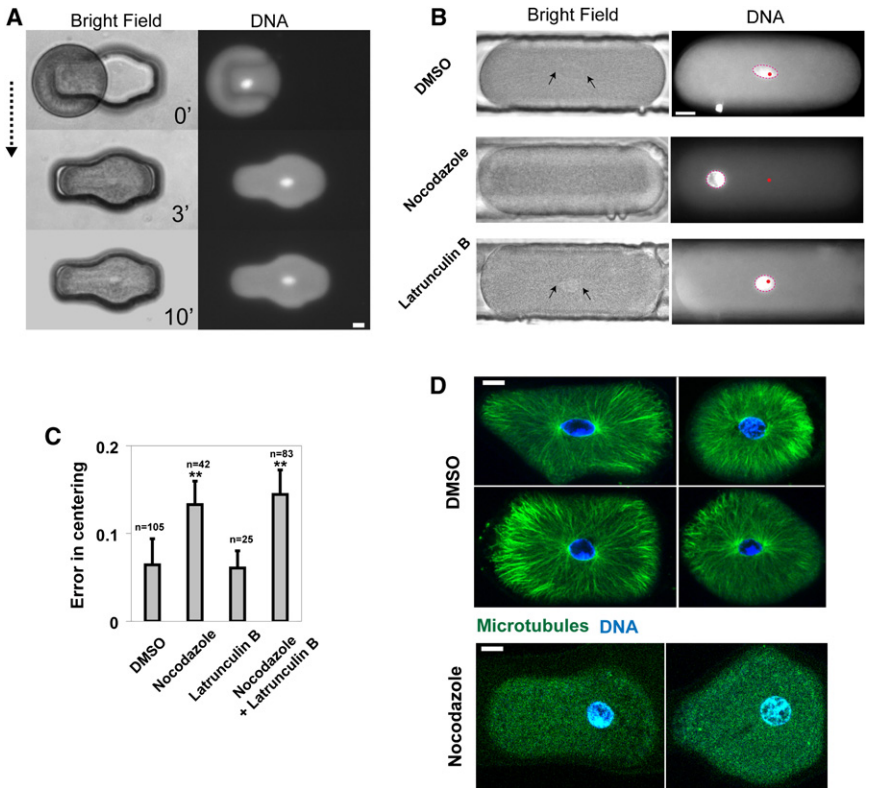

Figure 2. Nuclear Centering Is Microtubule Dependent

(A) Method for dynamically altering cell shape. Images of an interphase cell before and after entry into a well. The nucleus, stained with Hoechst, is positioned at the new cell center within minutes.

(B) Images of interphase cells a few minutes after being pushed into chambers in the presence of 1% DMSO (control), 20 μM nocodazole, or 20 μM Latrunculin B (from top to bottom). Black arrows point to asters adjacent to the nucleus. The cell center of mass is marked by a red dot, and the nucleus is outlined in purple.

(C) Quantification of nuclear position in the indicated conditions. The error in centering is defined as the ratio between the distances from the nucleus center to the cell's center of mass to the long axis of the cell. Error bars represent standard deviations.

(D) Confocal images of cells in chambers fixed and stained in situ for tubulin (green) and DNA (blue), in the presence of 1% DMSO or 20 μM nocodazole. Images are projections of Z stacks of 20 mid-section slices that cover a total depth of 10 μm.

**p < 0.01, Student's t test compared with the control. Scale bars, 20 μm. See also Figure S3.

formed in a plane perpendicular to this axis (Figures 1D and 1E, Figure S2A, and Movie S1). Importantly, the furrow did not appear to reorient or reposition during contraction (Figure S2B). After cytokinesis, however, adhesion forces between the two daughter cells sometimes led to a minor (usually < 5–10°) reorientation of the initial division axis. Computer-aided measurements showed that the position of the interphase nucleus predicted the position of the mitotic spindle and the subsequent division plane (to within 5% of the cell's radius on average), and that orientation of the interphase nucleus also predicted the orientation of the spindle and division plane (within 10% on average) (Figure 1E). Together these data suggested that the division position and axis relative to a given geometry are set by the orientation of the nucleus during interphase or early prophase.

Nuclear Centering Is Dependent on Microtubules and Not Actin

The microtubule and actin cytoskeletons have been implicated in positioning and orienting the nucleus and spindle in various cell types and contexts (Carminati and Stearns, 1997; Grill et al., 2001; Schuh and Ellenberg, 2008; Tran et al., 2001). In normal urchin zygotes, interphase microtubules (MTs) are organized in two asters nucleated from two diametrically opposed zones around the nucleus (Foe and von Dassow, 2008; Holy and Schatten, 1997). F-actin appears relatively diffuse throughout the cytoplasm and is enhanced at the cell surface (Wong et al., 1997). Inhibition of MTs with nocodazole or F-actin with Latrunculin B blocks pronuclei migration or entry into mitosis, depending on the time of addition (data not shown) (Hamaguchi and Hiramoto, 1986; Schatten et al., 1986). To investigate the mechanism of nuclear centering, after pronuclear fusion, we pushed cells into chambers to dynamically alter their cell shape and then assayed for the ability of the nucleus to center relative to this new shape (Figure 2A). In control cells, the nucleus recentered at the new center of mass in less than 1–2 min (Figures 2A–2C). Addition of 20 μM nocodazole prior to the cell shape change inhibited recentering of the nucleus (Figures 2B and 2C); this nocadozole treatment led to the depolymerization of detectable MTs at this stage (Figure 2D). Depolymerization of F-actin with 20 μM Latrunculin B did not affect the process (Figure 2C and Figure S3C). Thus, nuclear centering depends on microtubules and not actin in this cell type.

The Nucleus Acts as a Force Sensor

We observed that nuclear shape was elongated along an axis that predicts the future spindle axis. The nucleus elongated along the new long axis in less than 3 min after the change in cell shape (Figure 2A). Nocodazole treatment prior to the shape change abolished nuclear elongation and gave rise to a spherical nucleus (Figures 2B and 2D and Figure 3A). Treatment with 20 μM Latrunculin B had a minor but significant effect on the nuclear aspect ratio (Figure 2B and Figure 3A). Depolymerization of both MTs and actin was similar to treatment with nocodazole alone, suggesting that these effects were not additive. Latrunculin B did not grossly affect MT distribution (Figure S3D). Based upon work in other cell types, F-actin could contribute to multiple aspects of nuclear elongation, including

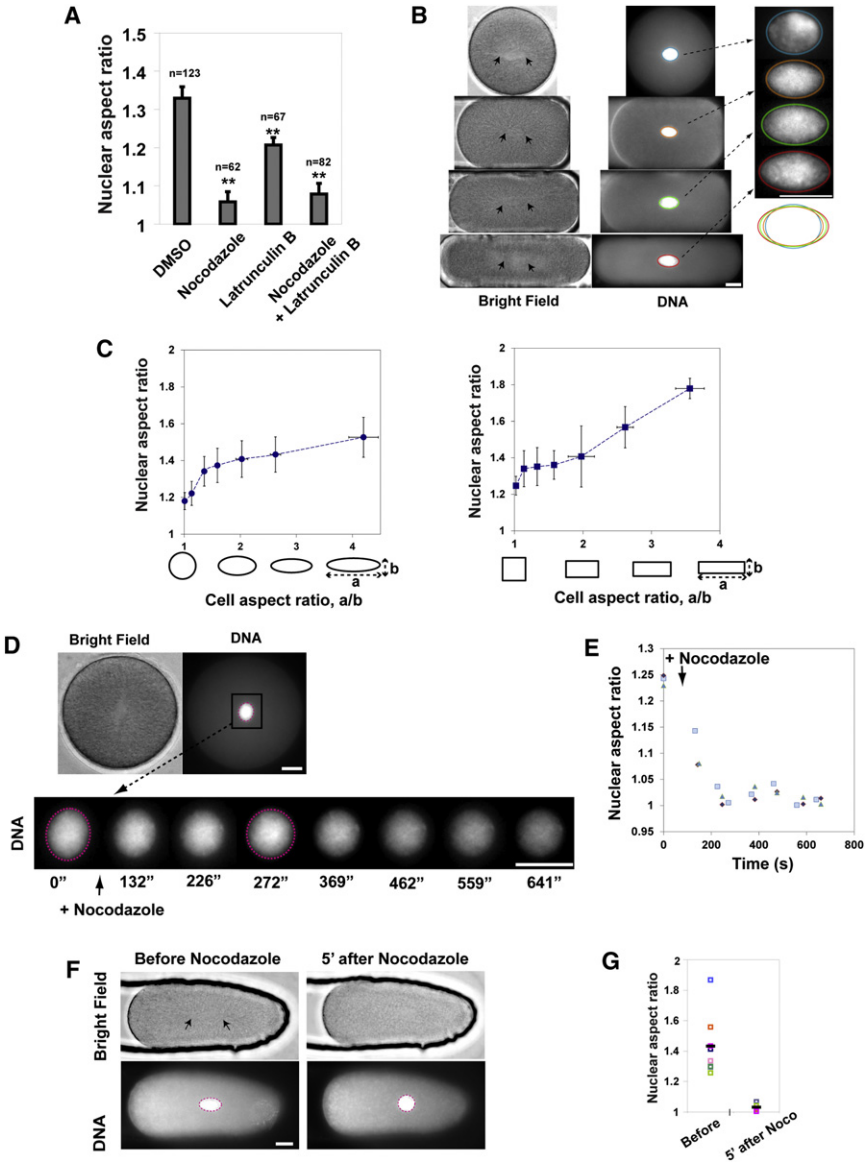

Figure 3. Nuclear Shape Is an Indicator of Microtubule Pulling Forces

(A) Quantification of nuclear shape in cells treated with the indicated drugs (as in Figure 2B). The nuclear aspect ratio is defined as the ratio between the long and short axis of the ellipsoid shape of the nucleus. The cells used for this quantification have a geometrical aspect ratio smaller than 1.5 (see 3C). Error bars represent standard deviations.

(B) Nuclear shape in cells with increasing aspect ratios. Close-up images of nuclei in different cells are presented on the right. Dotted colored lines outline each nucleus. Their superimposition highlights the increase in nuclear aspect ratio as cells are more elongated. Black arrows in the bright-field picture point at aster centers on the side of the nucleus.

(C) Plot of the nuclear aspect ratio as a function of the cell aspect ratio, a/b, for a series of ellipsoid and rectangular cell shapes. Each point is binned from data on 10 or more cells having the same shape, for a total number of 104 cells for the ellipses and 82 for the rectangles. Error bars represent standard deviations. The dotted lines are depicted to guide the eyes.

(D) Time-lapse images of the interphase nucleus in a cell just prior to and after treatment with 20 μM nocodazole. Note that nuclear shape becomes spherical in minutes.

(E) The nuclear aspect ratio as a function of time in the representative cell in Figure 2D and two other cells treated in the same manner.

(F) Effect of 20 μM nocadozole on the nuclear shape in elongated cells inside chambers. Black arrows point at aster centers on the side of the nucleus and the dotted purple lines outline the nucleus.

(G) Nuclear aspect ratio in cells inside chambers before and after treatment with 20 μM nocodazole (1 cell per color, n = 8 cells). The black horizontal bar represents the mean value.

**p < 0.01, Student's t test compared with the control. Scale bars, 20 μm.

the linking of the centrosomes to the nuclear envelope, mechanical properties of the nucleus, and the ability of MT motors to pull (Bettinger et al., 2004; Kunda and Baum, 2009). In these urchin cells, MTs provide the primary force that elongates the nucleus, with actin providing a minor contribution.

We found that nuclear elongation was more pronounced in cells with elongated cell shapes (Figure 3B). We examined this correlation in a series of ellipsoidal and rectangular cells with increasing aspects ratios. Quantitation of the nuclear and cell aspect ratios showed a significant positive correlation between these parameters in both of these classes of shapes ($R^2 = 0.88$ and 0.98 for ellipses and rectangles, respectively).

We considered whether the degree of nuclear elongation could correspond to a stretching force exerted on the nucleus. Previous biophysical measurements have shown that the nucleus in *Xenopus* behaves as an elastic material with a defined elastic surface modulus of 25 pN/μm (Dahl et al., 2004). Nocodazole treatment caused the elongated nuclear shape to become spherical within 5 min (Figures 3D–3G). This effect was independent of initial nuclear aspect ratio. This behavior illustrates the elastic nature of the nucleus and the absence of plasticity (Dahl et al., 2004, 2008; Vaziri and Mofrad, 2007). These results indicate that MTs exert forces to stretch the elastic nucleus along the long axis of the cell, and that these forces scale with the aspect ratio of the cell shape.

Estimates of MT forces on the nuclear envelope can be obtained by representing the nucleus as a spherical thin elastic shell of elastic surface modulus K and radius r_N. The force necessary to deform such sphere into a prolate spheroid of aspect ratio

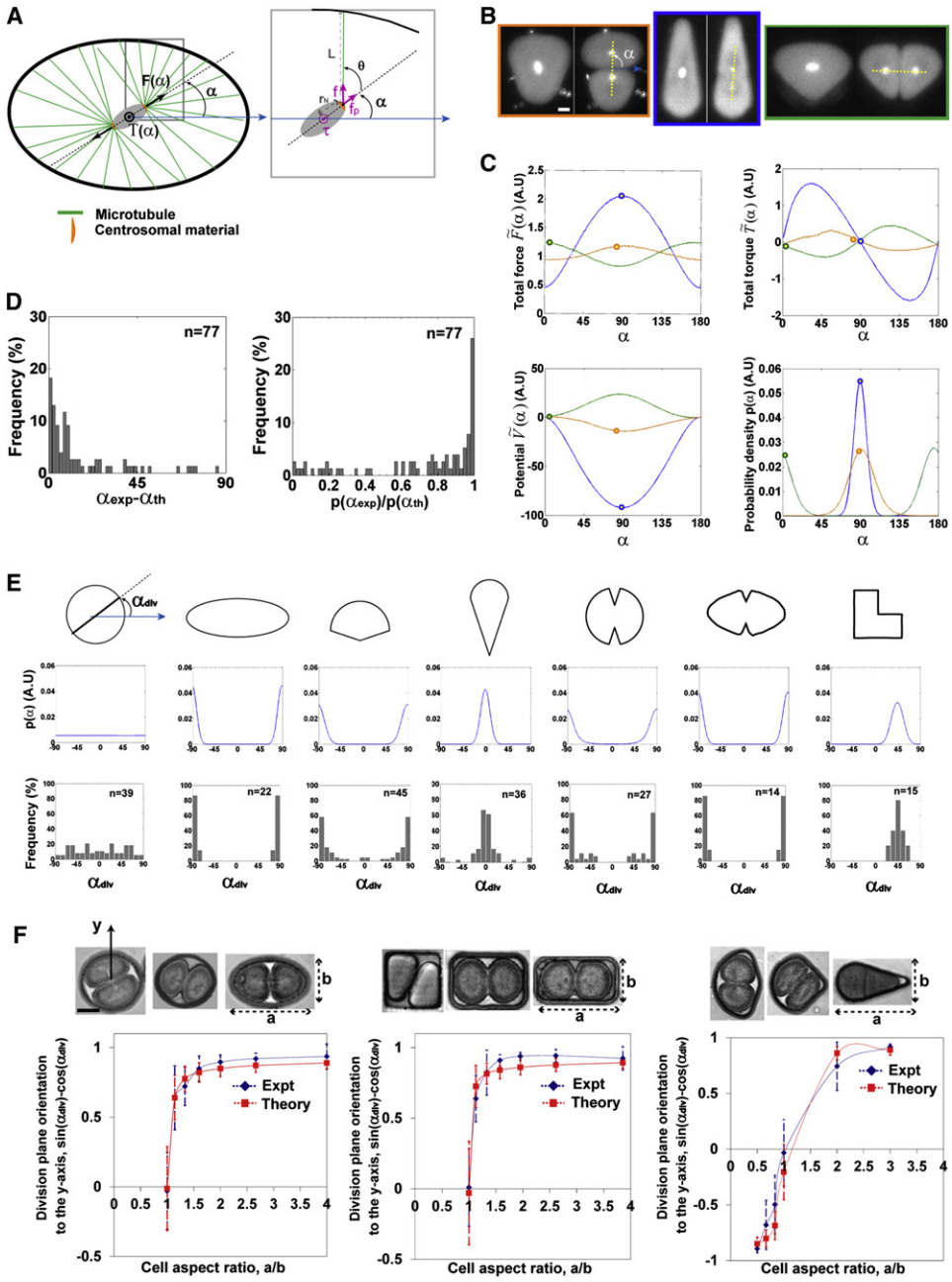

Figure 4. A Computational Model that Predicts Nuclear Orientation and Division-Plane Orientation in Response to Cell Geometry

(A) Schematic 2D representation of the cellular organization used for modeling. The nucleus (gray) is located at the center of mass and oriented along an axis α. Microtubules (green) emanate from two centrosomes (orange) attached to each side of the nucleus and extend out to the cortex. The total force generated by the two MT asters along the α axis is F(α), and the total torque at the cell's center is T(α). Inset: A microtubule in the aster has a length L and is nucleated at an angle θ from the axis α. It produces a pulling force f at its nuclear attachment and a torque τ at the nucleus center. The projection of the force along the axis α is denoted f_p.

(B) Examples of cells in specific geometries (triangles and fan) at interphase and after cytokinesis, stained with Hoechst. The nuclear and subsequent spindle orientation, α, is reported and highlighted by the yellow dotted line.

(C) The plots represent the different outputs of the model for these three cells in (B) (corresponding colors). The dots on the plots position the experimental spindle orientation α_{exp}. Note that in the three cases, α_{exp} is close to maxima of the total normalized force and the probability density, to zeros of the total normalized torque, and to minima of the normalized potential.

(D) (Left) Frequency histogram of the absolute difference between α_{exp} and α_{th} (calculated as the maxima of the probability density) for 77 dividing cells with different shapes. (Right) Frequency histogram of the probability density ratio for the same 77 sequences. The ratio is 1 when the experimental axis has the same probability density as the theoretical axis and 0 when the experimental axis falls in the zone where the probability density is 0.

(E) Model prediction of cleavage-plane orientation probability density in the depicted shapes and experimental frequency histograms of division axis in the depicted shape. Note that the division-plane angle used here, α_{div}, is rotated 90° from the nuclear orientation angle α presented in panels A–D.

ρ_N is given by (see supplemental model, Extended Experimental Procedures):

$$F = \frac{K}{1+\nu}\frac{r_N}{\ln(r_N/r_C)}\left(\rho_N^{2/3}-1\right), \quad (1)$$

where υ is the Poisson ratio of the material and r_C is the radius of the force application zone. If we assume that the elastic surface modulus of the sea urchin nucleus is similar to that of the *Xenopus* nucleus, our calculations estimate that the MT-dependent forces on the nucleus range from 10 to 30 pN, depending on the shape of the cell.

Microtubule Organization in Different Cell Shapes

We next examined the distribution of the interphase microtubules responsible for nuclear positioning. Bright-field images show that during interphase, the nucleus is associated with two asters, one on each side of the nucleus (Figure 2B and Figures 3B and 3F). To examine MTs directly, we performed immunostaining of tubulin in cells in the chambers (Figures S3A and S3B; see Experimental Procedures). In all shapes observed, MT staining confirmed the bipolar aster organization around the nucleus (Figure 2D and Figure S3E). MTs filled the whole volume of the cell and extended out to the cortex, even in elongated cells. They appeared to emanate from the centrosome at a relatively constant angular density, and the complete aster extended out over a little more than 180° (Figure S3F). In general, MTs did not exhibit buckling or curling around the cortex. In some cases there appeared to be increased tubulin staining, often near the cortex and regions of cell elongation. This pattern may be an artifact of fixation, in which some regions of the cells may be fixed unevenly due to staining in the chambers (Figure 2D and Figure S3E); alternatively, it may represent true increased local density of MTs in these regions. Although MT probes for imaging MT organization in live cells have been recently described, that study used injection of esconsin mRNA to assay 8-cell-stage embryos (von Dassow et al., 2009); our preliminary attempts to inject live 1-cell embryos in chambers with labeled esconsin protein, without modifying their shape, have not been successful (data not shown). The distribution of MTs throughout the cytoplasm and cortex suggest that MTs may directly probe the whole cell surface or volume for shape sensing.

The stretching of the nucleus and the lack of MT buckling strongly suggest that MTs are providing pulling forces on the nucleus (Figure 2D and Figure S3E). Although MT pushing, which results from MT polymerization, is a major factor in smaller cells such as fission yeast (Dogterom and Yurke, 1997; Tran et al., 2001), it may be only a minor component in these larger cells (Wuhr et al., 2009).

Computational Models for Microtubule-Based Shape Sensing

To understand how microtubules may globally sense cell shape for nuclear positioning, we developed quantitative models. The model aims to compute the forces and torques generated by MTs on the nucleus during interphase and output the probability of a given orientation of the division axis in a given geometry (Thery et al., 2007). We use a two-dimensional representation in which MTs emanate from two points diametrically opposed around the nucleus, grow straight, and reach out the cortex. Each microtubule produces a pulling force, f, on its nuclear attachment site and a torque, τ, at the nucleus center (Figure 4A).

A necessary input of the model is to assume that the force generated by each microtubule, f, depends on its length L (the exact nature of this dependence is discussed and tested below). Through this assumption, it can be shown that the nucleus will be centered near the cytoplasmic center of mass (Bjerknes, 1986; Howard, 2006). Thus, in what follows, the nucleus is assumed to be centered at the center of mass of the geometry, and we focus our attention on describing how cell shape affects axis orientation.

For each shape, we aim to compute the global force F and torque T generated as a function of the orientation angle of the stretched nuclear axis, α (Figure 4A). For each possible orientation α (α varying from 0 to π), we generate two asters of N MTs nucleated at a constant angular density ρ from centrosomes placed at a distance $\pm r_N$ from the cell's center of mass along the axis α. An MT orientated along the direction $\alpha+\theta$ has a length $L(\alpha,\theta)$ and generates a pulling force $f(L(\alpha,\theta))$ on its nuclear attachment that we project on the axis α, to compute the noncompensated force f_p:

$$f_p(\alpha,\theta) = f(L(\alpha,\theta))\cos(\theta). \quad (2)$$

The resultant total force $F(\alpha)$ generated by each aster on its nuclear attachment along the axis α is then obtained by summing the projected force over all MTs:

$$F(\alpha) = \int_{-\frac{\Phi}{2}}^{\frac{\Phi}{2}} f(L(\alpha,\theta))\cos(\theta)\rho d\theta, \quad (3)$$

where Φ is the total angular width of the aster. The torque created by each MT at the center of mass O and projected along the z axis is in turn computed as:

$$\tau(\alpha,\theta) = r_N f(L(\alpha,\theta))\sin(\theta), \quad (4)$$

which yields a total torque, $T(\alpha)$,

$$T(\alpha) = r_N \int_{-\frac{\Phi}{2}}^{\frac{\Phi}{2}} f(L(\alpha,\theta))\sin(\theta)\rho d\theta. \quad (5)$$

Initial tests of the model showed that, above a certain threshold, the number of MTs N (or equivalently the angular density: $\rho = N/\Phi$) does not impact axis definition but only affects the time required to align along this axis (see below). Thus, in what follows, we keep N as a silent parameter by normalizing

(F) (Top) DIC images of divided eggs in different geometry. (Bottom) Plot of the experimental and theoretical division-plane orientation to the *y* axis, $\sin(\alpha_{div})-\cos(\alpha_{div})$, as a function of the geometrical aspect ratio. The orientation to the *y* axis is −1 if all cells cleave perpendicular to the *y* axis, 1 if they all cleave parallel to the *y* axis, and 0 for a random distribution of cleavage planes. Each experimental point is averaged on at least 15 different cells in a given shape. Error bars represent standard deviations. Scale bars, 20 μm. See also Figure S4, Figure S5, and Table S1.

the total force and torque with the total force computed in a round normal cell, F_0: $\tilde{F}(\alpha)=F(\alpha)/F_0$ and $\tilde{T}(\alpha)=T(\alpha)/(r_N F_0)$. These normalized parameters have no units and are independent of MT number. Stable axis orientation can be identified from local minima of the normalized potential $\tilde{V}(\alpha)$ computed as a primitive of $\tilde{T}(\alpha)$. The probability density associated with each orientation $p(\alpha)$ is then calculated by introducing a white noise in the distribution of torques as proposed in Thery et al. (2007),

$$p(\alpha)=p_0\exp\left(-\frac{\tilde{V}(\alpha)}{C}\right). \quad (7)$$

In this formula, p_0 is adjusted so that $\int p(\alpha)=1$ and C is a dimensionless fitting parameter that includes noise strength and nuclear friction (Thery et al., 2007). The parameter C is fitted by dichotomy to match the experimental average orientation in an ellipse with a small aspect ratio (see Figure 4F). This C value, as well as the geometrical parameters, r_N and Φ, and the total force F_0 are then fixed in all simulations presented hereafter, so that the only input that varies through different simulations is the geometry of the cell (see supplemental model, Extended Experimental Procedures and Table S1).

As examples, we present the results of two triangles and an elongated fan-like shape, for which we plot $\tilde{F}(\alpha), \tilde{T}(\alpha), \tilde{V}(\alpha)$ and $p(\alpha)$ (Figures 4B and 4C). In these cases, the theoretical orientation angle α_{th}, which is calculated at the highest predicted orientation probability, was within 5%–10% of the experimental orientation angle α_{exp} measured at anaphase.

Testing the Model for Different Shapes

We compared theoretical predictions and experimental results of time-lapse sequences of cells in many different shapes. In general, the theoretical predictions closely approximated the experimental results. In a large dataset of 77 cells of assorted shapes, the average difference between the experimental and theoretical angle α_{exp} and α_{th} was 15.6° ± 10.0° (Figure 4D). In addition, we also tested whether the model predicts the probability that a specific orientation will be chosen. In shapes where length differences between different axes are small (a circle), a large difference between theoretical and experimental angles could be obtained whereas the difference in probability density is close to 0, as all orientations have an equal probability. The average ratio between the theoretical and experimental probability densities obtained from the same set of 77 cells was 0.72 ± 0.16 (Figure 4D).

We also compared sets of division-plane data for each individual cell shape (Figure 4E). In each shape, the computed probability density quantitatively correlated with the experimental division-plane orientation frequency. Thus, the model was highly successful in predicting the division-plane orientations.

Testing the Sensitivity of Shape Sensing

We sought to determine how sensitive a cell is in sensing its shape. We generated series of datasets in which the aspect ratios of the shape were systematically altered (Figure 4F). The simplest case is a series covering the transition from a circle to ellipses with increasing aspect ratio. As expected, the division axis was purely random in a circular cell. Shaping a cell into an ellipse with an aspect ratio as small as 1.15, however, was sufficient to significantly bias the division orientation perpendicular to the long axis. At higher aspect ratios, the average orientation saturated, and the standard deviation decreased. Similar results were seen in the transition from a square to rectangles. Another informative case consisted of varying the ratio between the two major axes of a fan-like shape, in which the transition between two orthogonal division axes can be examined. This transition showed a sharp slope at the point where the two axes have similar length, supporting the view that the shape-sensing mechanism is finely tuned. These results demonstrate that the cell can robustly sense fine differences in aspect ratio of less than 15%.

In all cases, the results of the theoretical model using a single set of fixed parameters matched the experimental data with remarkable accuracy in predicting the average orientation, the standard deviation, and the precision in sensing shape. Thus this simple model, which improves upon Hertwig's long axis rule, demonstrates that length-dependent MT forces can account for spindle orientation and cell shape sensing.

Testing Mechanisms of Microtubule-Dependent Forces

MT pulling forces can be generated through minus-end-directed motors such as cytoplasmic dynein that may interact with the cortex and/or with cytoplasmic elements that serve as a putative "cytoplasmic scaffold" (Carminati and Stearns, 1997; Gonczy et al., 1999; Hamaguchi and Hiramoto, 1986; Kimura and Onami, 2005; O'Connell and Wang, 2000; Wuhr et al., 2010). We considered various models that differ in the location and density of MT pulling motors. One distinguishing hallmark between these models is how the force scales with MT length L (Hays et al., 1982) . For instance, in a model in which motors are attached to the cortex and are in limiting concentration, the MT force is predicted to scale approximately with L^2 (Grill and Hyman, 2005; Hara and Kimura, 2009; Howard, 2006). In a model in which motors are uniformly attached to the cytoplasmic matrix, the pulling force may scale with L. Thus, to test mechanisms of length-dependent forces, we used a general scaling law with the form of $f(L) \sim L^{\beta}$ and sought to determine an experimental value of the exponent β.

This β value could be estimated by comparing our experimental data on nuclear stretching with theoretical pulling forces exerted by MTs. We focused on the data series of ellipsoid and rectangular shapes with increasing aspect ratio (Figure 3B). In both of these types of shapes, the preferred axis orientation corresponds to α = 0 and to the maximum total force as well, $\tilde{F}_{max}=\tilde{F}(\alpha=0)$ (Figure 5). We thus computed for different values of β the evolution of $\tilde{F}_{max}$ as a function of the aspect ratio a/b, in ellipses and rectangles (see different color plots in Figure 5), and calculated what value of β fits best the experimental behavior (see supplemental model, Extended Experimental Procedures). This approach leads to exponent values for each dataset: β_{ell} = 3.1 ± 0.9 and β_{rect} = 3.4 ± 1.5. Integrating MT forces on a 3D volume led to estimates of exponents of 4 to 4.5 (see supplemental model, Extended Experimental Procedures). Thus, these two independent datasets show that MT forces roughly scale with L to the power of 3 to 5. This measurement indicates nonlinearity in these MT length-scaling forces. This analysis rules out

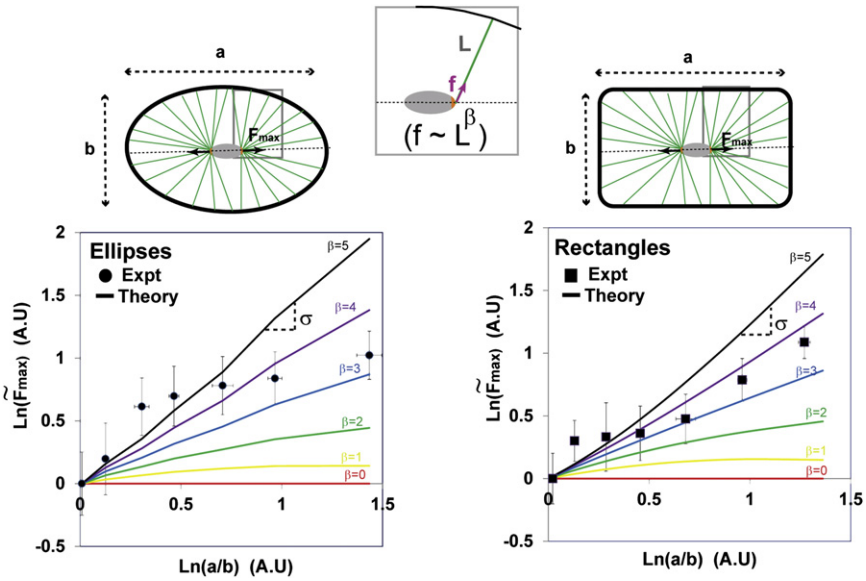

Figure 5. Nuclear Force Scaling in Different Shapes Reveals Length Dependency of Microtubules Forces

(Top) Schematic 2D representation of the cellular organization used for force scaling modeling in the series of ellipses and rectangles. The axis orientation is fixed at the stable orientation, $\alpha = 0$, which also corresponds to the maximum force, F_{max}. Inset: The MT pulling force, f, is set to be proportional to L^{β}. (Bottom) Logarithmic plots of the normalized total force as a function of the cell aspect ratio. The experimental maximum forces are computed using Equation 1 from the nuclear aspect ratio data reported in Figure 3C and normalized to the force in a round cell. Theoretical plots are generated for different values of β (different colors). The slope σ is computed from fitting each plot linearly. Error bars represent standard deviations.

certain mechanisms, such as a simple model where cytoplasmic-anchored motors saturate the MT lattice, and suggests mechanisms that incorporate more complex length dependency (see Discussion).

We also tested whether these different power laws could affect orientation axis, by comparing experimental division-axis distribution with theoretical density probability plots generated with different β values (Figure S4). This comparison showed that axis orientation was independent of β (for $\beta > 0$) and suggested that neither the total force intensity nor the detailed scaling of the force-generation system are critical for steady-state orientation (see also Figure 7). We additionally tested another proposed shape-sensing mechanism based on contact-angle-dependent MT forces (Tsou et al., 2003) and found that it was not consistent with our experimental results in some shapes (Figure S4).

Predicting Division Axis in Multicellular Contexts

To test the generality of this model, we examined whether it could predict division planes in multicellular, developmental contexts. First, we used it to predict division positions in subsequent embryonic divisions in the sea urchin. We followed the behavior of urchin embryos through multiple divisions as they were confined in PDMS chambers of different geometries (Figure 6A). Cells were shaped by contact with the wall of the chamber and by other cells in the chamber. We used our model to predict the division planes based solely upon cell shapes and found that the theoretical predictions were in excellent agreement with the experimental findings: the average difference between the experimental and theoretical division-plane orientation angle was 11.5° ± 9.1° and the mean ratio of theoretical to experimental probability densities was 0.82 ± 0.12.

We note that these experiments mimic geometrical effects during embryonic development in different organisms, in which the chamber can be regarded as an artificial egg shell that constrains and shapes the dividing cells. A circular chamber corresponds, for instance, to the situation for most deuterosomes including humans and urchins, as well as the animal pole view of meroblastic cleavages of *Xenopus* or Zebrafish eggs. An ellipsoidal chamber is similar to a mouse embryo or an embryo of the nematode *Prionchulus*, which exhibits initial symmetric cleavages (Schierenberg, 2006). The division planes with sea urchin blastomeres in the chambers reproduced with excellent fidelity the observed patterns of initial blastula divisions seen in these diverse organisms. Although cell-cell contact has been considered to provide spindle orientation cues (Goldstein, 1995; Wang et al., 1997), we noted that in certain shaped chambers (like triangles and elongated rectangles), spindle orientation did not correlate with the orientation of the first cleavage plane and thus appeared to be governed in these situations more by cell shape cues than by putative cell-cell contact signals.

Next, we asked whether our model could predict spindle axis orientation within an adult tissue. Figure 6B depicts an illustration of a tissue section from the pigeon testis (Guyer, 1900), which shows the shape and spindle orientation of spermatocytes undergoing meiosis. From this image, we traced the geometry of each cell and simulated the probability density distribution of spindle orientations. Our model was able to predict the division planes accurately: the average difference between the experimental and theoretical spindle orientation angle was 8.5° ± 3.1°, and the mean ratio of theoretical to experimental probability densities was 0.79 ± 0.22 (n = 13). Thus, in these cells, spindle orientation may be determined by geometrical cues. These findings demonstrate how this model may be generally applicable in predicting division patterns and illustrate how cell shape can be a major parameter in defining cleavage patterns during development.

Shape Sensing in Spindle Reorientation

In many cell types, the spindle undergoes rotation during metaphase or anaphase. Although the spindle does not normally rotate, in these early divisions in sea urchins (Figure 1), we tested

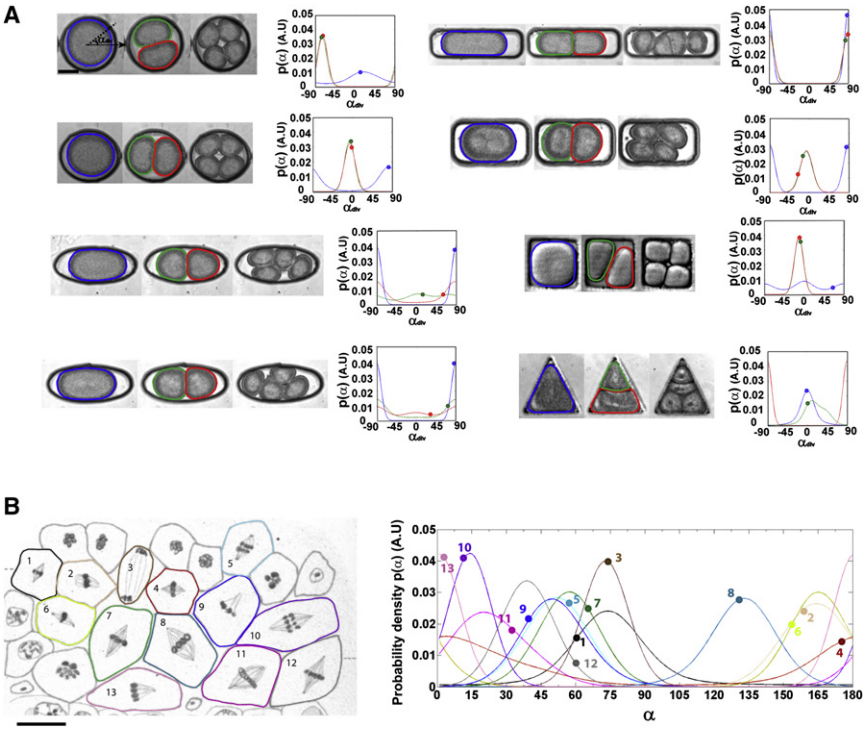

Figure 6. Predicting Embryonic Cleavage Patterns and Spindle Orientation in Tissues

(A) Time-lapse images of urchin embryos going through the first two cleavages encased in chambers of different geometries. Each colored graph on the right corresponds to the predicted probability density computed from the shape of the cell on the left, contoured with the same color. The color blue is used for the zygote, and green and red are used for the 2-cell blastomeres. The spots on the plots correspond to the experimental division-plane axis. Note that the division-plane angle used here, $\alpha_{div,}$ is rotated 90° from the nuclear orientation angle α presented in Figures 4A–4D.

(B) Drawing of meiotic spermatocytes with different shapes from a tissue section of the pigeon testis, reprinted from Guyer (1900). The corresponding computed theoretical spindle orientation probability density is plotted on the right in the corresponding color and number. Only cells depicting a spindle in the image plane are analyzed.

The spots on the plots correspond to the experimental axis. Scale bars, 20 μm.

whether it could reorient upon a change in cell shape. We arrested urchin embryos in metaphase by treatment with the proteasome inhibitor MG132 and introduced them into chambers of different shapes. We observed that the metaphase spindle reoriented along an axis defined by the new cell shape (Figures 7A–7E and Figure S6). The relatively slow rotation allowed us to analyze this movement using time-lapse imaging. Rotations occurred in a relatively unidirectional and steady movement and occurred in 3 to 30 min depending on the initial axis orientation and the geometry. Spindles that were properly aligned initially did not exhibit rotations or oscillations. This process depended on microtubules but not on actin (Figures 7C, 7D, and 7E). The slow timescale for this rotation as compared to the interphase nucleus, which orients in less than 3 min (Figure 2A), suggested that the torque intensity generated by MTs was much smaller in metaphase (see supplemental model, Extended Experimental Procedures). We studied this movement using our computational model (Figure 7F), using an identical set of parameters (except for MT number, see below) and an estimate of friction of the nucleus and spindle in the cytoplasm (see supplemental model, Extended Experimental Procedures). The results of the simulations correlated well with experimental findings (Figure 7B and Figure S6). The best overall fit in the model occurred if we assumed that metaphase spindles have only around 0.6% of the number of effective MTs of the interphase arrays (at which the ratio of interphase to metaphase number of MTs is around 150; Figure 7G). The calculation is consistent with immunofluorescence images showing very few astral MTs contacting the cortex in these cells (Figures 7C and 7D) (Strickland et al., 2005). Thus, this model is applicable to spindle orientation as well as nuclear orientation. Further, this example demonstrates how this model can be used to analyze parameters such as the rate of orientation and the number of effective MTs.

DISCUSSION

A Model for Orienting the Division Axis Relative to Cell Shape

By systematically studying the effects of changing cell shape, we develop and test a simple quantitative model for how cell geometry dictates the positioning and orientation of the nucleus and spindle, which subsequently positions the cleavage furrow. MTs emanating from centrosomes on the nucleus probe the dimensions of the cell and exert pulling forces that depend on MT length. The observed elongation of the nuclear envelope provides estimated forces on the order of 10–30 pN on the nuclear envelope, which scales with the aspect ratio of the cell. This force, which may represent a time average of a more dynamic molecular organization, corresponds to a relatively small number of force generators (around 10–50), as seen in other systems (Grill et al., 2003). Through modeling, we demonstrate that such length-dependent MT forces are sufficient to explain nuclear centering and orientation in these cells; more elaborate mechanisms involving intracellular gradients (Moseley and Nurse, 2010) or actin-based mechanisms (Kunda and Baum, 2009) are not needed. The cell may thus sense its shape primarily by "measuring" the length of its MTs that extend from the centrosome to the cell surface. Integration of these forces over the whole cell provides a mechanical ensemble that seeks to reach equilibrium.

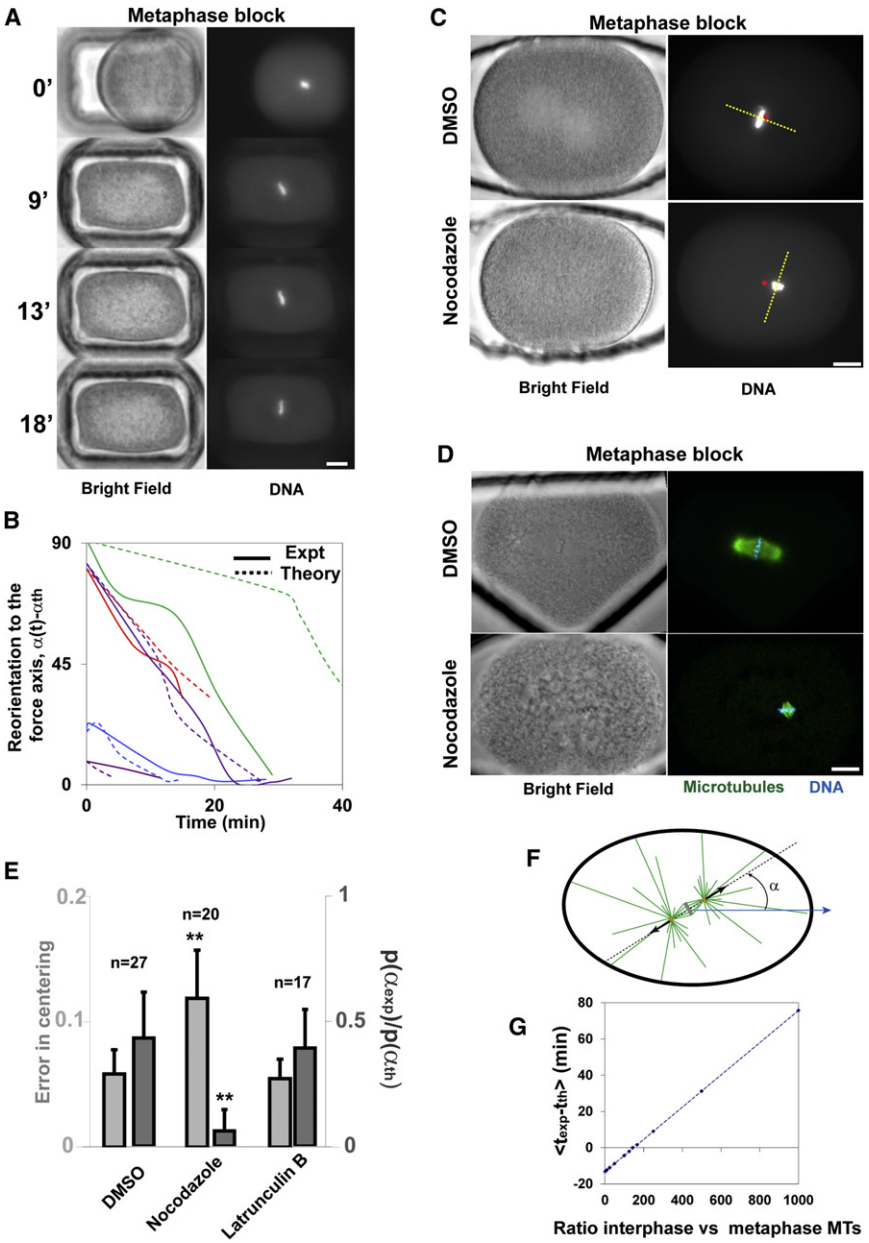

Figure 7. Rotation of the Metaphase Spindle in Response to Cell-Shape Changes

(A) Cells were blocked in metaphase by treatment with the inhibitor MG132 and then changed into a new shape by introducing them into a well. Time-lapse images of spindle rotation (as shown by Hoechst staining) in a metaphase-arrested cell in a rectangular chamber are shown.

(B) Examples of experimental and theoretical plots of the reorientation of the spindle axis to the theoretical force axis. The theoretical plots are computed by assuming a ratio of metaphase to interphase MT number of 1/150 (see Figure 5G).

(C) Images of embryos blocked in metaphase and introduced into a chamber for 20 min, in the presence and in the absence of 20 μM nocodazole. The red point corresponds to the cell's center of mass and the yellow dotted line corresponds to the spindle axis.

(D) Confocal images of embryos blocked in metaphase, treated with 1% DMSO or 20 μM nocodazole and introduced into a chamber. After 20 min, cells were fixed and stained in situ for tubulin (green) and DNA (blue). Images are projections of Z stacks of 20 mid-section slices that cover a total depth of 10 μm.

(E) Quantification of spindle centering and orientation along the theoretical force axis in response to shape changes, in the indicated conditions. The error in centering is defined as the ratio between the distances from the metaphase spindle center to the cell's center of mass to the long axis of the cell. The orientation ratio, $p(\alpha_{exp})/p(\alpha_{th})$, is 1 when the spindle axis has the same probability density as the theoretical axis and 0 when the spindle axis falls in the zone where the probability density is 0. Error bars represent standard deviations.

(F) Schematic 2D representation of the cellular organization at metaphase.

(G) Average error between experimental and theoretical times corresponding to 12 different cells, plotted as a function of the ratio of metaphase to interphase MT number. A positive number corresponds to an underestimation in the reorientation timing of the model whereas a negative number corresponds to an overestimation of the model.

**$p < 0.01$, Student's t test compared with the control. Scale bars, 20 μm. See also Figure S6.

Our theoretical model is kept as simple as possible and deliberately infers only fixed adjustable parameters, modeling all cells in different geometries in the exact same manner. The exceptional fit between our experimental data and theoretical model for a wide variety of different shapes indicates that this process is close to the theoretical limit. Our model can readily predict spindle orientation with good accuracy in other cell types and thus promises to be adaptable for predicting division orientations in many cell types in a broad variety of contexts. Cell-type-specific parameters such as the relative sizes of the cell and nuclei, as well as MT organization, could even be optimized to provide the best predictability (Figure S5). These rules may apply best to cells in which cell geometry itself plays a primary role in determining the axis of division. In addition, this model could be valuable to predict whether a given cell uses cell geometry as a primary cue and to analyze parameters in the system, such as effective MT number.

Microtubule Length-Dependent Forces

A key aspect of our model is the assumption that MTs exert forces that scale with MT length. Recent progress has begun to reveal molecular details of how such length-dependent forces could occur through interactions with MT motors such as dynein or depolymerizing kinesin (Gardner et al., 2008; Tischer et al.,

2009; Varga et al., 2009; Vogel et al., 2009). For instance, a long MT may accumulate or contact more MT pulling motors than a short one. In considering different mechanisms, an open question is whether MT forces are being generated directly by pulling motors attached on cytoplasmic elements or at the cortex (Grill and Hyman, 2005; Reinsch and Gonczy, 1998; Wuhr et al., 2009). Studies in *Xenopus* and sand dollar embryos show that centering mechanisms can function even if the MTs do not contact the cortex, suggesting that cytoplasmic pulling is a possible mechanism in these large cells (Hamaguchi and Hiramoto, 1986; Wuhr et al., 2010). Motors may be situated in the cytoplasm, for instance on some internal membrane component or some putative cytoplasmic "matrix." Alternatively, motors may primarily associate on the MT lattice and travel to accumulate at the plus ends.

Although technical limitations in the sea urchin system have limited the ability to directly image motors in this process, our experimental data coupled with computational modeling allow us to discriminate between some proposed mechanisms. Our results estimate that the forces scale in a nonlinear manner to MT length (L) to roughly L^3. This finding is not consistent with basic linear models in which the number of force-generating elements is strictly proportional to MT length. One previously proposed nonlinear scaling can result from having a limited number of motors at the cortex, which pull on a fraction of astral MTs (Grill and Hyman, 2005; Howard, 2006). This view makes the aster "surface sensitive" and is equivalent to a force per MT scaling with L^2 (Hara and Kimura, 2009). We propose a "volume sensing" model that is more consistent with our scaling close to the L^3: motors, which are in limited numbers in the cytoplasm, encounter a given MT of length L with a probability that is proportional to the cone-shaped unit volume surrounding the MT.

Additional dynamic sources of nonlinear length scaling may be positive feedback or cooperativity among multiple mechanisms. For instance, longer MTs might accumulate more motors not only because of their increased length but also because of their long lifetime (Seetapun and Odde, 2010), which can lead to increased tubulin posttranslational modifications that can help recruit more motors and increase accumulation of MT stability factors (Cai et al., 2009). Another potential factor may be the increased probability of new nucleation of noncentrosomal MTs off of longer pre-existing MTs (Janson et al., 2007). Further quantitative analysis of MTs and associated motors will help to test these proposed models.

EXPERIMENTAL PROCEDURES

Microchamber Fabrication and Operation

Chambers containing the arrays of microwells were fabricated by rapid prototyping and PDMS technology as described in Minc et al. (2009a), Minc et al. (2009b), and Velve-Casquillas et al. (2010). A SU-8-positive master containing hundreds of posts that are 70 μm in height and of different geometries was first made by microlithography (Figure S1A). A 10:1 mixture of PDMS Sylgard 184 silicone elastomer and curing agent was poured onto the master and baked at 65°C for 4 hr. The replica was cut, peeled off the master, and activated with a plasma cleaner (Harrick Plasma). A 100 μl drop of fertilized eggs in sea water was placed onto the PDMS replica and the eggs were left to sediment by gravity for 2 min. A 22 mm^2 glass coverslip was then placed on top of the suspension, and water was gently sucked from the sides of the coverslip with a kimwipe, which slowly pushed the eggs into the chambers. To perfuse cells inside chambers, for in situ immunofluorescence or drug treatment, we used an inverse set-up: The PDMS replica was first pierced with two large holes. The drop of eggs was placed onto a 45 × 50 mm^2 large coverslip and subsequently covered with the PDMS replica. Water was removed, as before, to reduce the space between the PDMS and the coverslip, which caused the eggs to adopt the shape of the microchamber (Figure S3A). Buffers, drugs, or fixatives were added slowly through the large holes and removed by sucking from the side of the PDMS replica. Cells were monitored on the microscope to ensure that no major shape change was occurring. For incubation periods longer than 1 hr the whole chamber was placed in a sealed box filled with some wet paper to limit drying. Rapid nocodazole treatment on normal spherical eggs was performed in a different set of microfluidic channels designed as in Minc and Chang (2010).

Collection and Fertilization of Sea Urchin Eggs

Lytechinus pictus sea urchins were purchased from Marinus Scientific. Gametes were collected by intracoelemic injection of 0.5M KCl. The eggs were resuspended and gently agitated twice in fresh sea water. Sperm were diluted 1000-fold in sea water, activated by vigorous aeration, and then added dropwise to the eggs. Fertilization was monitored after 2 min. Fertilization envelopes were subsequently removed by pouring the eggs through Nitex mesh in sea water with 5 mM PABA (4-Aminobenzoic acid). The cells were maintained at 17°C–19°C throughout the experiment.

Pharmacological Inhibitors and Dyes

The DNA stain Hoechst 33342 (Molecular Probes) was added at a final concentration of 1 μg/ml after the fertilization envelopes were removed. Inhibitors were added at appropriate periods of the cell cycle and incubated 5 min prior to observation. Nocodazole was used at a final concentration of 20 μM from a 100× stock solution made fresh in DMSO. Latrunculin B (Sigma) was used at a final concentration of 20 μM from a 100× stock in DMSO. MG132 (Sigma) was added to the eggs 30 min before fertilization at a final concentration of 50 μM from a 100× stock in DMSO.

Fixation and Staining Procedure

Fixation and staining procedures were adapted from Foe and von Dassow (2008) and Strickland et al. (2004). Briefly, cells were fixed in 100 mM HEPES (pH 6.9), 50 mM EGTA, 10 mM $MgSO_4$, 2% formaldehyde, 0.2% glutaraldehyde, 0.2% acrolein, 0.2% Triton X-100, and 400 mM dextrose for 45 min. Cells were then rinsed three times in PBT, treated with 0.1% $NaBH_4$ in PBS to limit autofluorescence for 30 min, and finally blocked in 5% goat serum for 1 hr. Microtubule staining was performed using a primary anti-α-tubulin antibody, clone DM 1A (Sigma) at 1/8000 incubated overnight and a CY3-conjugated anti-mouse secondary antibody at 1/750 (Sigma) incubated during 5 hr. Actin staining was performed using Alexa fluor phalloidin (Molecular Probes) incubated during 1 hr.

Microscopy and Image Analysis

Microscopy was performed with an inverted wide-field fluorescence microscope with a motorized stage (Ludl Instrument). The objectives used were either a 10× 0.25 NA or a 40× 0.75 NA. Confocal imaging of microtubules was performed with a laser-scanning confocal microscope (LSM 710, Zeiss) with a 40× 1.3 NA oil objective. Images were acquired, processed, and analyzed with OpenLab (Improvision), Micro-manager, Image J, Zen (Zeiss), and Matlab (Mathworks).

Computational Modeling

All computational simulations were performed using Matlab (Mathworks). Scripts can be made available upon request. Details and tests of the different used models are provided in the Extended Experimental Procedures.

SUPPLEMENTAL INFORMATION

Supplemental Information includes Extended Experimental Procedures, six figures, one table, and one movie and can be found with this article online at doi:10.1016/j.cell.2011.01.016.

ACKNOWLEDGMENTS

The authors acknowledge all members of the Chang and Burgess laboratories for discussions and technical assistance. We thank A. Boudaoud for careful reading of the manuscript and J. Brill for discussions. Microfabrication was made in the Columbia CEPSR clean room. Part of the microscopy was performed in the Microbiology Department confocal microscopy facility. This work, which was initiated at the Marine Biological Laboratory, was supported by National Institutes of Health (NIH) RO1 grants GM069670 and GM056836 and an Ellison Senior Scholar award to F.C. N.M. acknowledges support from the CNRS and an ANR "retour post-doctorants" grant ANR-10PDOC-003-01. The authors dedicate this manuscript to the memory of Ray Rappaport.

Received: May 25, 2010
Revised: November 9, 2010
Accepted: January 10, 2011
Published: February 3, 2011

REFERENCES

Bettinger, B.T., Gilbert, D.M., and Amberg, D.C. (2004). Actin up in the nucleus. Nat. Rev. Mol. Cell Biol. *5*, 410–415.

Bjerknes, M. (1986). Physical theory of the orientation of astral mitotic spindles. Science *234*, 1413–1416.

Cai, D., McEwen, D.P., Martens, J.R., Meyhofer, E., and Verhey, K.J. (2009). Single molecule imaging reveals differences in microtubule track selection between Kinesin motors. PLoS Biol. *7*, e1000216.

Carminati, J.L., and Stearns, T. (1997). Microtubules orient the mitotic spindle in yeast through dynein-dependent interactions with the cell cortex. J. Cell Biol. *138*, 629–641.

Concha, M.L., and Adams, R.J. (1998). Oriented cell divisions and cellular morphogenesis in the zebrafish gastrula and neurula: a time-lapse analysis. Development *125*, 983–994.

Dahl, K.N., Kahn, S.M., Wilson, K.L., and Discher, D.E. (2004). The nuclear envelope lamina network has elasticity and a compressibility limit suggestive of a molecular shock absorber. J. Cell Sci. *117*, 4779–4786.

Dahl, K.N., Ribeiro, A.J., and Lammerding, J. (2008). Nuclear shape, mechanics, and mechanotransduction. Circ. Res. *102*, 1307–1318.

Dogterom, M., and Yurke, B. (1997). Measurement of the force-velocity relation for growing microtubules. Science *278*, 856–860.

Foe, V.E., and von Dassow, G. (2008). Stable and dynamic microtubules coordinately shape the myosin activation zone during cytokinetic furrow formation. J. Cell Biol. *183*, 457–470.

Gardner, M.K., Bouck, D.C., Paliulis, L.V., Meehl, J.B., O'Toole, E.T., Haase, J., Soubry, A., Joglekar, A.P., Winey, M., Salmon, E.D., et al. (2008). Chromosome congression by Kinesin-5 motor-mediated disassembly of longer kinetochore microtubules. Cell *135*, 894–906.

Goldstein, B. (1995). Cell contacts orient some cell division axes in the Caenorhabditis elegans embryo. J. Cell Biol. *129*, 1071–1080.

Gonczy, P., Pichler, S., Kirkham, M., and Hyman, A.A. (1999). Cytoplasmic dynein is required for distinct aspects of MTOC positioning, including centrosome separation, in the one cell stage Caenorhabditis elegans embryo. J. Cell Biol. *147*, 135–150.

Gray, D., Plusa, B., Piotrowska, K., Na, J., Tom, B., Glover, D.M., and Zernicka-Goetz, M. (2004). First cleavage of the mouse embryo responds to change in egg shape at fertilization. Curr. Biol. *14*, 397–405.

Grill, S.W., and Hyman, A.A. (2005). Spindle positioning by cortical pulling forces. Dev. Cell *8*, 461–465.

Grill, S.W., Gonczy, P., Stelzer, E.H., and Hyman, A.A. (2001). Polarity controls forces governing asymmetric spindle positioning in the Caenorhabditis elegans embryo. Nature *409*, 630–633.

Grill, S.W., Howard, J., Schaffer, E., Stelzer, E.H., and Hyman, A.A. (2003). The distribution of active force generators controls mitotic spindle position. Science *301*, 518–521.

Guyer, M.F. (1900). Spermatogenesis of normal and of hybrid pigeons. A dissertation, (Chicago, IL: The University of Chicago). http://post.queensu.ca/~forsdyke/guyer01.htm.

Hamaguchi, M.S., and Hiramoto, Y. (1986). Analysis of the role of astral rays in pronuclear migration in sand dollar eggs by the colcemid-UV method. Dev. Growth Differ. *28*, 143–156.

Hara, Y., and Kimura, A. (2009). Cell-size-dependent spindle elongation in the *Caenorhabditis elegans* early embryo. Curr. Biol. *19*, 1549–1554.

Hays, T.S., Wise, D., and Salmon, E.D. (1982). Traction force on a kinetochore at metaphase acts as a linear function of kinetochore fiber length. J. Cell Biol. *93*, 374–389.

Hertwig, O. (1884). Das Problem der Befruchtung une der Isotropie des Eies, eine Theory der Vererbung (Jenaische Zeitschrist).

Holy, J., and Schatten, G. (1997). Recruitment of maternal material during assembly of the zygote centrosome in fertilized sea urchin eggs. Cell Tissue Res. *289*, 285–297.

Howard, J. (2006). Elastic and damping forces generated by confined arrays of dynamic microtubules. Phys. Biol. *3*, 54–66.

Janson, M.E., Loughlin, R., Loiodice, I., Fu, C., Brunner, D., Nedelec, F.J., and Tran, P.T. (2007). Crosslinkers and motors organize dynamic microtubules to form stable bipolar arrays in fission yeast. Cell *128*, 357–368.

Jenkinson, J.W. (1909). Experimental Embryology (Oxford, UK: Clarendon Press).

Kimura, A., and Onami, S. (2005). Computer simulations and image processing reveal length-dependent pulling force as the primary mechanism for *C. elegans* male pronuclear migration. Dev. Cell *8*, 765–775.

Kunda, P., and Baum, B. (2009). The actin cytoskeleton in spindle assembly and positioning. Trends Cell Biol. *19*, 174–179.

Minc, N., Boudaoud, A., and Chang, F. (2009a). Mechanical forces of fission yeast growth. Curr. Biol. *19*, 1096–1101.

Minc, N., Bratman, S.V., Basu, R., and Chang, F. (2009b). Establishing new sites of polarization by microtubules. Curr. Biol. *19*, 83–94.

Minc, N., and Chang, F. (2010). Electrical control of cell polarization in the fission yeast *Schizosaccharomyces pombe*. Curr. Biol. *20*, 710–716.

Moseley, J.B., and Nurse, P. (2010). Cell division intersects with cell geometry. Cell *142*, 184–188.

O'Connell, C.B., and Wang, Y.L. (2000). Mammalian spindle orientation and position respond to changes in cell shape in a dynein-dependent fashion. Mol. Biol. Cell *11*, 1765–1774.

Rappaport, R. (1996). Cytokinesis in Animal Cells (Cambridge, UK: Cambridge University Press).

Reinsch, S., and Gonczy, P. (1998). Mechanisms of nuclear positioning. J. Cell Sci. *111*, 2283–2295.

Schatten, G., Schatten, H., Spector, I., Cline, C., Paweletz, N., Simerly, C., and Petzelt, C. (1986). Latrunculin inhibits the microfilament-mediated processes during fertilization, cleavage and early development in sea urchins and mice. Exp. Cell Res. *166*, 191–208.

Schierenberg, E. (2006). Embryological variation during nematode development. WormBook *2006*, 1–13.

Schuh, M., and Ellenberg, J. (2008). A new model for asymmetric spindle positioning in mouse oocytes. Curr. Biol. *18*, 1986–1992.

Seetapun, D., and Odde, D.J. (2010). Cell-length-dependent microtubule accumulation during polarization. Curr. Biol. *20*, 979–988.

Strauss, B., Adams, R.J., and Papalopulu, N. (2006). A default mechanism of spindle orientation based on cell shape is sufficient to generate cell fate diversity in polarised Xenopus blastomeres. Development *133*, 3883–3893.

Strickland, L., von Dassow, G., Ellenberg, J., Foe, V., Lenart, P., and Burgess, D. (2004). Light microscopy of echinoderm embryos. Methods Cell Biol. *74*, 371–409.

Strickland, L.I., Wen, Y., Gundersen, G.G., and Burgess, D.R. (2005). Interaction between EB1 and p150glued is required for anaphase astral microtubule elongation and stimulation of cytokinesis. Curr. Biol. *15*, 2249–2255.

Thery, M., and Bornens, M. (2006). Cell shape and cell division. Curr. Opin. Cell Biol. *18*, 648–657.

Thery, M., Jimenez-Dalmaroni, A., Racine, V., Bornens, M., and Julicher, F. (2007). Experimental and theoretical study of mitotic spindle orientation. Nature *447*, 493–496.

Thery, M., Racine, V., Pepin, A., Piel, M., Chen, Y., Sibarita, J.B., and Bornens, M. (2005). The extracellular matrix guides the orientation of the cell division axis. Nat. Cell Biol. *7*, 947–953.

Tischer, C., Brunner, D., and Dogterom, M. (2009). Force- and kinesin-8-dependent effects in the spatial regulation of fission yeast microtubule dynamics. Mol. Syst. Biol. *5*, 250.

Tran, P.T., Marsh, L., Doye, V., Inoue, S., and Chang, F. (2001). A mechanism for nuclear positioning in fission yeast based on microtubule pushing. J. Cell Biol. *153*, 397–411.

Tsou, M.F., Ku, W., Hayashi, A., and Rose, L.S. (2003). PAR-dependent and geometry-dependent mechanisms of spindle positioning. J. Cell Biol. *160*, 845–855.

Varga, V., Leduc, C., Bormuth, V., Diez, S., and Howard, J. (2009). Kinesin-8 motors act cooperatively to mediate length-dependent microtubule depolymerization. Cell *138*, 1174–1183.

Vaziri, A., and Mofrad, M.R. (2007). Mechanics and deformation of the nucleus in micropipette aspiration experiment. J. Biomech. *40*, 2053–2062.

Velve-Casquillas, G., Le Berre, M., Piel, M., and Tran, P.T. (2010). Microfluidic tools for cell biological research. Nano Today *5*, 28–47.

Vogel, S.K., Pavin, N., Maghelli, N., Julicher, F., and Tolic-Norrelykke, I.M. (2009). Self-organization of dynein motors generates meiotic nuclear oscillations. PLoS Biol. *7*, e1000087.

von Dassow, G., Verbrugghe, K.J., Miller, A.L., Sider, J.R., and Bement, W.M. (2009). Action at a distance during cytokinesis. J. Cell Biol. *187*, 831–845.

Wang, S.W., Griffin, F.J., and Clark, W.H., Jr. (1997). Cell-cell association directed mitotic spindle orientation in the early development of the marine shrimp Sicyonia ingentis. Development *124*, 773–780.

Wong, G.K., Allen, P.G., and Begg, D.A. (1997). Dynamics of filamentous actin organization in the sea urchin egg cortex during early cleavage divisions: implications for the mechanism of cytokinesis. Cell Motil. Cytoskeleton *36*, 30–42.

Wuhr, M., Dumont, S., Groen, A.C., Needleman, D.J., and Mitchison, T.J. (2009). How does a millimeter-sized cell find its center? Cell Cycle *8*, 1115–1121.

Wuhr, M., Tan, E.S., Parker, S.K., Detrich, H.W., 3rd, and Mitchison, T.J. (2010). A model for cleavage plane determination in early amphibian and fish embryos. Curr. Biol. *20*, 2040–2045.